Computers and Structures 173 (2016) 161–173

Contents lists available at ScienceDirect

Computers and Structures

journal homepage: www.elsevier.com/locate/compstruc

The method of finite spheres in three-dimensional linear static analysis

Benjamin Lai *, Klaus-Jürgen Bathe

Massachusetts Institute of Technology, Cambridge, MA 02139, United States

ARTICLE INFO

Article history:
Received 17 February 2016
Accepted 30 May 2016
Available online 6 July 2016

Keywords:
Method of finite spheres
Meshless method
Three-dimensional linear elasticity
Partition of unity
Numerical integration
Computational cost

ABSTRACT

The objective of this paper is to assess the reliability and effectiveness of the method of finite spheres, a truly meshless overlapping finite element method, for the solution of practical three-dimensional linear elasticity problems. Advantages include simplified discretization and the elimination of element distortion. The method is implemented in the ADINA finite element program through a user-supplied element subroutine. The solutions of three increasingly complex three-dimensional problems are studied (1) to establish the reliability of the method for practical linear elasticity problems and (2) to assess the effectiveness of the method as compared to the standard finite element method. The solutions indicate that the method of finite spheres is between one and two orders of magnitude more expensive in computational time than the standard finite element method. This is still a promising result since there are significant time savings for the method of finite spheres during the pre-processing phase, particularly in the discretization of complicated three-dimensional geometries and because the overlapping sphere elements can be directly coupled to traditional finite elements.

1. Introduction

The method of finite spheres is a truly meshless overlapping finite element method developed to overcome the challenges in mesh-based numerical methods. In the finite element method, challenges include mesh generation for geometrically complex domains, avoidance of severe element distortions, and mesh alignment and refinement for modeling problems with discontinuities and singularities [1]. Mesh generation is time-consuming and requires special attention to remove distorted elements, especially for complex three-dimensional domains. Element distortion causes a loss of predictive capability since the element is no longer able to represent the same order of polynomials, leading to inaccuracies in numerical integration and an overall loss of reliability and solution accuracy [2]. In the method of finite spheres, overlapping sphere elements simplify the discretization of complex three-dimensional domains and eliminate the risk of distorted elements.

The challenges in mesh-based numerical methods have attracted substantial research efforts, leading to the development of numerous meshless methods [3–5]. Some of the most prominent meshless methods include smoothed particle hydrodynamics (SPH), the diffuse element method (DEM), the element-free Galerkin method (EFG), and the meshless local Petrov–Galerkin method (MLPG). The method of finite spheres (MFS) inherently possesses the advantages of meshless methods, and can also be thought of as a reliable and efficient finite element method using overlapping elements.

Smoothed particle hydrodynamics, one of the earliest developments in meshless methods, was originally used to model astrophysical phenomena. The method has since been implemented for a wide range of practical engineering applications, predominantly in the area of computational fluid dynamics, but also with extensions to solid mechanics. Despite the inherent advantages of being a meshless Lagrangian particle method, SPH possesses some numerical complications such as tensile instability and spurious boundary effects, which can lead to poor accuracy in the solution. Furthermore, generally a large number of particles and the use of adjustable solution factors are required to obtain reasonable accuracy, reducing the efficiency and robustness of the method. Several modifications and corrections have been proposed to restore consistency and accuracy of SPH, but further research efforts are necessary before the method can be regarded as robust and efficient for practical applications [6,7].

The diffuse element method was the first of many meshless methods based on the Galerkin formulation. The method uses moving least squares (MLS) to generate smooth approximations based on a set of discretization points. Since DEM is a global weak form method, a background mesh is required for numerical integration, suggesting the method is only meshless with regard to constructing interpolation functions. Furthermore, there are a number of oversimplifications which affect the validity of the

* Corresponding author.
E-mail address: benlai@mit.edu (B. Lai).

http://dx.doi.org/10.1016/j.compstruc.2016.05.023
0045-7949/

method. In particular, the derivative of the approximation functions is evaluated only approximately, a very low quadrature rule for numerical integration is applied, and the Dirichlet boundary conditions are not accurately enforced. Consequently, DEM does not pass the patch test and fails consistency requirements [8].

The element-free Galerkin method is an extension of DEM, introducing a series of improvements which results in a more accurate formulation at the expense of increased computational cost. Specifically, EFG correctly evaluates the derivatives of the approximation functions, employs a larger number of integration points in the numerical integration procedure, and utilizes Lagrange multipliers to accurately enforce the Dirichlet boundary conditions. The EFG method also uses MLS approximations to construct the trial and test functions which provides reasonable accuracy, but requires an expensive matrix inversion at every integration point. Furthermore, there is an additional condition that at every integration point there is a minimum number of domains of influence that must have nonzero support. These complications concerning matrix inversion and overlap significantly reduce the computational efficiency of the method [9–12].

The meshless local Petrov–Galerkin method is a concept that can adopt trial and test functions from different approximation spaces, resulting in various formulations which offer flexibility to deal with different boundary value problems. Various formulations of the MLPG approach have been used to solve three-dimensional elastostatics problems, using different test functions, such as the Heaviside function or the Dirac delta function, and different approximations, based on radial basis functions or moving least squares. Unlike DEM and EFG, the MLPG method works with a local weak form instead of a global weak form, which means that numerical integration is performed over local subdomains rather than using a background mesh or cell structure. Therefore, it is a truly meshless method since a mesh is not required for either interpolation or integration. However, with the approximation functions based on the MLS approximation, the method suffers from the same complications as DEM and EFG [13–15].

Although a variety of meshless techniques have been developed, the currently available reliable methods are much more expensive than the finite element method and come with various complications that affect their overall effectiveness. The method of finite spheres incorporates advantages of the finite element method and meshless methods and focuses on being both reliable and computationally efficient. Early research demonstrated the reliability of MFS for one- and two-dimensional linear analysis of solids and fluids. Further research established a mixed displacement/pressure formulation, improved numerical integration, finite element coupling, enrichment strategies, automatic discretization, genetic algorithms for numerical integration, and a scheme for the analysis of wave propagation problems [16–25].

The focus of this paper is on assessing the reliability and efficiency of the method of finite spheres for the analysis of practical three-dimensional linear elastic problems, where the traditional finite element method suffers from costly mesh generation and errors resulting from element distortions. In Section 2, we develop the theory and formulation of the method of finite spheres and present an effective local approximation space for constructing three-dimensional interpolation functions. Thereafter, in Section 3, we propose a simple numerical integration scheme known as the piecewise Gauss–Legendre quadrature rule for the integration of the nonpolynomial functions over the three-dimensional spherical domains. In Section 4, we discuss our implementation of the method of finite spheres in a user element subroutine of ADINA. Then in Section 5, we study the solutions of three increasingly more complex three-dimensional analysis problems in order to establish the reliability and assess the efficiency of MFS for practical linear elastic analysis. Lastly, in Section 6, we summarize the major developments and discuss possible further research toward improving the efficiency of the method.

2. Formulation of the method of finite spheres

In this section we present the theory and formulation of the method of finite spheres for three-dimensional linear elasticity problems. The presentation is largely based on Ref. [16].

2.1. Sphere discretization

Consider a general three-dimensional domain V with domain boundary $S = S_u \cup S_f$, where S_u is the Dirichlet boundary and S_f is the Neumann boundary. The unit normal to the domain boundary, $\underline{n}$, is positive in the outward direction. Let $\{B(\underline{x}_I, r_I);\ I = 1, \ldots, N\}$ be a set of spheres, where $\underline{x}_I$ and r_I refer to the center coordinates and radius of sphere B_I, respectively, and where I is the nodal label of each sphere and N is the total number of spheres. As illustrated in Fig. 1, spheres can be classified as either an interior or boundary sphere.

The requirements for a valid sphere discretization are (1) all sphere centers must be within the domain, (2) the domain must be completely covered by the union of all spheres, and (3) no sphere can be completely included in any other sphere. Discretization depends only on the position vector and radius of the spheres. With overlapping elements, the method of finite spheres avoids discretization difficulties and element distortion.

2.2. Interpolation scheme

The interpolation scheme for the method of finite spheres is based on the partition of unity paradigm [26–28]. Interpolation functions are defined as the product of Shepard functions and local basis functions. An effective local approximation space is chosen for three-dimensional linear elasticity problems.

2.2.1. Shepard partition of unity functions

The Shepard partition of unity functions are given by

$$\varphi_I^0(\underline{x}) = \frac{W_I}{\sum_{J=1}^{N} W_J}, \quad I = 1, \ldots, N \tag{1}$$

where $W_I(\underline{x})$ denotes a positive radial weighting function. The Shepard functions are nonpolynomial and have zeroth-order consistency, ensuring that rigid body modes can be reproduced exactly. The choice of weighting function should consider the continuity class and the ease of differentiation and integration so that low-cost partitions of unity are obtained. We choose the quartic spline weighting function defined as

$$W_I(s) = \begin{cases} 1 - 6s^2 + 8s^3 - 3s^4, & 0 \leqslant s \leqslant 1 \\ 0, & s > 1 \end{cases} \tag{2}$$

where $s = (\|\underline{x} - \underline{x}_I\|)/r_I$.

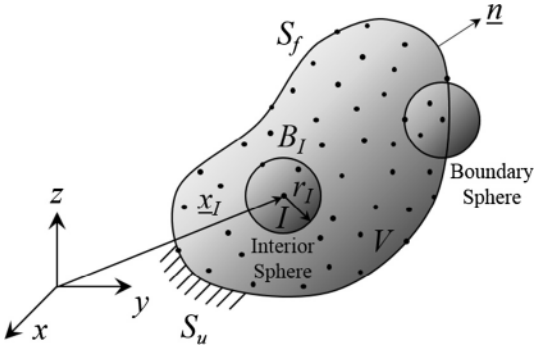

Fig. 1. General three-dimensional domain V with domain boundary $S = S_u \cup S_f$.

2.2.2. Approximation space

Since the Shepard partition of unity functions only satisfy zeroth-order consistency, a local approximation space $v_I^h = \text{span}_{m\in\mathcal{I}}\{p_m(\underline{x})\}$ is defined at each node I to generate approximation spaces of higher-order consistency, where h is a measure of the sphere size, $\mathcal{I}$ is an index set, and $p_m(\underline{x})$ is a member of the local basis. The global approximation space V_h is defined as the product of the Shepard function and the functions from the local basis

$$V_h = \sum_{I=1}^{N} \varphi_I^0 v_I^h \tag{3}$$

Hence any function v_h in the solution space v_h can be written as

$$v_h(\underline{x}) = \sum_{I=1}^{N}\sum_{m\in\mathcal{I}} h_{Im}(\underline{x})\alpha_{Im} \tag{4}$$

where the interpolation functions are defined as

$$h_{Im}(\underline{x}) = \varphi_I^0(\underline{x})p_m(\underline{x}) \tag{5}$$

and α_{Im} is the mth degree of freedom at node I. For three-dimensional linear elasticity problems, which are within the class of elliptic problems, a suitable local approximation space is

$$V_I^h = \text{span}\{1, \bar{x}, \bar{y}, \bar{z}, \bar{x}\bar{y}, \bar{y}\bar{z}, \bar{z}\bar{x}\} \tag{6}$$

which contains the terms of a complete first-order polynomial, where $\bar{x} = (x - x_I)/r_I$, $\bar{y} = (y - y_I)/r_I$, and $\bar{z} = (z - z_I)/r_I$.

Unlike in the standard finite element method, an effective local approximation space can be chosen for solving specific problems, improving the accuracy and efficiency of the method of finite spheres. For example, a local approximation space containing trigonometric functions is suitable for hyperbolic problems, which has been demonstrated for the dynamic analysis of wave propagations [25]. For the method of finite spheres, the choice of local approximation space is significant because it is advantageous to employ different interpolation functions for different classes of problems.

2.3. Displacement-based method of finite spheres

In this section, we present the formulation of the displacement-based method of finite spheres for three-dimensional linear elasticity problems.

2.3.1. Governing differential equations

The governing differential equations for a linear elastic continuum $V \in R^3$ with domain boundary S are

$$\underline{\partial}_\varepsilon^T \underline{\tau} + \underline{f}^B = \underline{0} \text{ in } V \tag{7}$$

with Neumann boundary conditions

$$\underline{N\tau} = \underline{f}^S \text{ on } S_f \tag{8}$$

and Dirichlet boundary conditions

$$\underline{u} = \underline{u}^S \text{ on } S_u \tag{9}$$

The strain–displacement relation is given by

$$\underline{\varepsilon} = \underline{\partial}_\varepsilon \underline{u} \tag{10}$$

and the linear elastic constitutive relation is given by

$$\underline{\tau} = \underline{C\varepsilon} \tag{11}$$

In Eqs. (7)–(11), $\underline{u}$ is the displacement vector, $\underline{\varepsilon}$ is the strain vector, $\underline{\tau}$ is the stress vector, $\underline{f}^B$ is the body force vector, $\underline{f}^S$ is the prescribed traction vector on the Neumann boundary S_f, $\underline{u}^S$ is the prescribed displacement vector on the Dirichlet boundary S_u, $\underline{\partial}_\varepsilon$ is a linear gradient operator, $\underline{N}$ is the direction cosine matrix for the unit normal to the domain boundary (positive outwards), and $\underline{C}$ is the elasticity matrix.

2.3.2. Variational formulation

For the linear elastic domain $V \in R^3$, the variational indicator is

$$\prod(\underline{u}) = \tfrac{1}{2}\int_V \underline{\varepsilon}^T(\underline{u})\underline{C\varepsilon}(\underline{u})dV - \Re \tag{12}$$

where the term $\Re$ accounts for the externally applied body forces, surface tractions, and prescribed displacements, given by

$$\Re = \int_V \underline{u}^T\underline{f}^B dV + \int_{S_f} \underline{u}^T\underline{f}^S dS + \int_{S_u} \underline{f}^{uT}(\underline{u} - \underline{u}^S)dS \tag{13}$$

and the traction vector $\underline{f}^u$ on the Dirichlet boundary may be expressed as

$$\underline{f}^u = \underline{NC\varepsilon}(\underline{u}) \tag{14}$$

By invoking the stationarity of the variational indicator Π in Eq. (12), we obtain the following weak form:

Find $\underline{u} \in H^1(V)$ such that

$$\begin{aligned}&\int_V \underline{\varepsilon}^T(\underline{v})\underline{C\varepsilon}(\underline{u})dV - \int_{S_u}[\underline{\varepsilon}^T(\underline{v})\underline{CN}^T\underline{u} + \underline{v}^T\underline{NC\varepsilon}(\underline{u})]dS \\ &= \int_V \underline{v}^T\underline{f}^B dV + \int_{S_f}\underline{v}^T\underline{f}^S dS - \int_{S_u}\underline{\varepsilon}^T(\underline{v})\underline{CN}^T\underline{u}^S dS \quad \forall \underline{v} \in H^1(V)\end{aligned} \tag{15}$$

where $H^1(V)$ is the first-order Hilbert space.

2.3.3. Nodal interpolations

For three-dimensional analysis, the displacement field approximation is

$$\underline{u}(x,y,z) = \begin{Bmatrix} u \\ v \\ w \end{Bmatrix} = \sum_{J=1}^{N}\sum_{n\in\mathcal{I}} \underline{H}_{Jn}(x,y,z)\underline{\alpha}_{Jn} = \underline{H}(x,y,z)\underline{U} \tag{16}$$

The corresponding strain field is

$$\underline{\varepsilon}(x,y,z) = \begin{Bmatrix} \varepsilon_{xx} \\ \varepsilon_{yy} \\ \varepsilon_{zz} \\ \gamma_{xy} \\ \gamma_{yz} \\ \gamma_{zx} \end{Bmatrix} = \sum_{J=1}^{N}\sum_{n\in\mathcal{I}} \underline{B}_{Jn}(x,y,z)\underline{\alpha}_{Jn} = \underline{B}(x,y,z)\underline{U} \tag{17}$$

and the corresponding stress field is

$$\underline{\tau}(x,y,z) = \begin{Bmatrix} \tau_{xx} \\ \tau_{yy} \\ \tau_{zz} \\ \tau_{xy} \\ \tau_{yz} \\ \tau_{zx} \end{Bmatrix} = \sum_{J=1}^{N}\sum_{n\in\mathcal{I}} \underline{CB}_{Jn}(x,y,z)\underline{\alpha}_{Jn} = \underline{CB}(x,y,z)\underline{U} \tag{18}$$

where $\underline{U} = [\underline{\alpha}_{11} \;\; \underline{\alpha}_{12} \;\; \cdots \;\; \underline{\alpha}_{Jn} \;\; \cdots]^T$ is the vector of nodal unknowns, $\underline{\alpha}_{Jn} = [u^{Jn} \;\; v^{Jn} \;\; w^{Jn}]$ is the vector of nodal unknowns at node J corresponding to the nth degree of freedom, and u^{Jn}, v^{Jn}, and w^{Jn} are the x-, y-, and z-displacements, respectively, at node J corresponding to the nth degree of freedom.

The displacement interpolation matrix is

$$\underline{H}_{Jn}(x,y,z) = \begin{bmatrix} h_{Jn} & 0 & 0 \\ 0 & h_{Jn} & 0 \\ 0 & 0 & h_{Jn} \end{bmatrix} \tag{19}$$

and the strain–displacement matrix is

$$\underline{B}_{Jn}(x,y,z) = \underline{\partial}_e \underline{H}_{Jn}(x,y,z) = \begin{bmatrix} \frac{\partial h_{Jn}}{\partial x} & 0 & 0 \\ 0 & \frac{\partial h_{Jn}}{\partial y} & 0 \\ 0 & 0 & \frac{\partial h_{Jn}}{\partial z} \\ \frac{\partial h_{Jn}}{\partial y} & \frac{\partial h_{Jn}}{\partial x} & 0 \\ 0 & \frac{\partial h_{Jn}}{\partial z} & \frac{\partial h_{Jn}}{\partial y} \\ \frac{\partial h_{Jn}}{\partial z} & 0 & \frac{\partial h_{Jn}}{\partial x} \end{bmatrix} \tag{20}$$

The elasticity matrix is given by

$$\underline{C} = \frac{E(1-\nu)}{(1+\nu)(1-2\nu)} \begin{bmatrix} 1 & \frac{\nu}{1-\nu} & \frac{\nu}{1-\nu} & 0 & 0 & 0 \\ \frac{\nu}{1-\nu} & 1 & \frac{\nu}{1-\nu} & 0 & 0 & 0 \\ \frac{\nu}{1-\nu} & \frac{\nu}{1-\nu} & 1 & 0 & 0 & 0 \\ 0 & 0 & 0 & \frac{1-2\nu}{2(1-\nu)} & 0 & 0 \\ 0 & 0 & 0 & 0 & \frac{1-2\nu}{2(1-\nu)} & 0 \\ 0 & 0 & 0 & 0 & 0 & \frac{1-2\nu}{2(1-\nu)} \end{bmatrix} \tag{21}$$

where E and ν are Young's modulus and Poisson's ratio of the material, respectively.

2.3.4. Discrete equilibrium equations

By substituting Eqs. (16)–(18) into Eq. (15), we obtain the discretized system of algebraic equations corresponding to node I and degree of freedom m

$$\sum_{J=1}^{N} \sum_{n \in \mathcal{I}} \underline{K}_{ImJn} \underline{\alpha}_{Jn} = \underline{f}_{Im} + \hat{\underline{f}}_{Im} \tag{22}$$

where the stiffness matrix is

$$\underline{K}_{ImJn} = \int_{V_I} \underline{B}_{Im}^T \underline{C} \underline{B}_{Jn} dV \tag{23}$$

and the body force load vector is

$$\underline{f}_{Im} = \int_{V_I} \underline{H}_{Im} \underline{f}^B dV \tag{24}$$

with $V_I = V \cap B(\underline{x}_I, r_I)$.

The traction force vector corresponding to node I and degree of freedom m is

$$\hat{\underline{f}}_{Im} = \begin{cases} \underline{0}, & \text{for an interior sphere} \\ \int_{S_{f_I}} \underline{H}_{Im} \underline{f}^S dS, & \text{for a Neumann boundary sphere} \\ \sum_{J=1}^{N} \sum_{n \in \mathcal{I}} \underline{KU}_{ImJn} \underline{\alpha}_{Jn} - \underline{fU}_{Im}, & \text{for a Dirichlet boundary sphere} \end{cases} \tag{25}$$

where

$$\underline{KU}_{ImJn} = \int_{S_{u_I}} \underline{H}_{Im} \underline{N} \underline{C} \underline{B}_{Jn} dS + \int_{S_{u_I}} \underline{B}_{Im}^T \underline{C} \underline{N}^T \underline{H}_{Jn} dS \tag{26}$$

and

$$\underline{fU}_{Im} = \int_{S_{u_I}} \underline{B}_{Im}^T \underline{C} \underline{N}^T \underline{u}^S dS \tag{27}$$

with $S_f = \cup_{I \in N_f} S_{f_I}$ where N_f is the index set of nodes with nonzero intercept on the Neumann boundary and $S_u = \cup_{I \in N_u} S_{u_I}$ where N_u is the index set of nodes with nonzero intercept on the Dirichlet boundary.

3. Numerical integration procedure

Numerical integration is a focal point of development for the method of finite spheres and for meshless methods in general [29–34]. Specialized integration schemes for the method of finite spheres have been developed in one- and two-dimensions [16–19]. In three-dimensions, the method requires integration of nonpolynomial functions over complicated integration domains, namely spheres, truncated spheres, and general lens-shaped regions for the overlap of spheres.

3.1. Sphere integration domains

In the method of finite spheres, the types of sphere integration domains encountered are classified as interior spheres, boundary spheres, and sphere overlap regions. In Fig. 2, we show these classifications, illustrating two-dimensional "spheres" or "disks" for simplicity, though three-dimensional spheres are implied.

3.2. Piecewise Gauss–Legendre quadrature rule

The piecewise Gauss–Legendre quadrature rule is a simple quadrature rule developed for the method of finite spheres. Each sphere domain is divided along the coordinate axes into eight subdomains. The standard Gauss–Legendre quadrature rule is applied in each of these subdomains, considering only the integration points that lie in the intersection of the sphere and the problem domain. The calculations are performed in the global coordinate system to avoid additional computations when using the natural coordinate system of a sphere element. Since the exact integration of complex nonpolynomial functions is not possible, the goal is to obtain a solution of sufficient accuracy using a minimum number of integration points.

Advantages of the piecewise Gauss–Legendre quadrature rule include a uniform density of integration points and direct integration of overlap regions. In the following sections we assume a constant radius for all spheres and we describe the piecewise Gauss–Legendre quadrature rule for each sphere integration domain, where as before, three-dimensional spheres are represented by two-dimensional "sphere" illustrations.

3.2.1. Interior sphere

An interior sphere divided by the coordinate axes is illustrated in Fig. 3. Within each subdomain, the standard Gauss–Legendre quadrature rule is employed. For an interior sphere, all points within the sphere contribute to the integration and are shown as red[1] points. By dividing the integration domain, the complexity of the integrand is reduced and accuracy is improved. Furthermore, there is a uniform density of integration points throughout the integration domain.

3.2.2. Boundary sphere

In Fig. 4, a boundary sphere is depicted where the problem domain is shaded in gray and the portion of the sphere which lies in the domain is shaded in blue. A Gauss–Legendre quadrature rule is considered in each subdomain, but only the integration points in the intersection of the sphere and the domain, denoted by red points, are used in the integration calculations.

3.2.3. Sphere overlap region

For a sphere overlap region, the same set of integration points considered for the interior sphere or boundary sphere are used. For example, we consider the sphere overlap region illustrated in Fig. 2c with the coordinate system centered on the left interior sphere, shown in Fig. 5. The standard Gauss–Legendre quadrature rule is considered in each subdomain, and from this set of integra-

[1] For interpretation of color in Figs. 3–5, 14, 20, and 26, the reader is referred to the web version of this article.

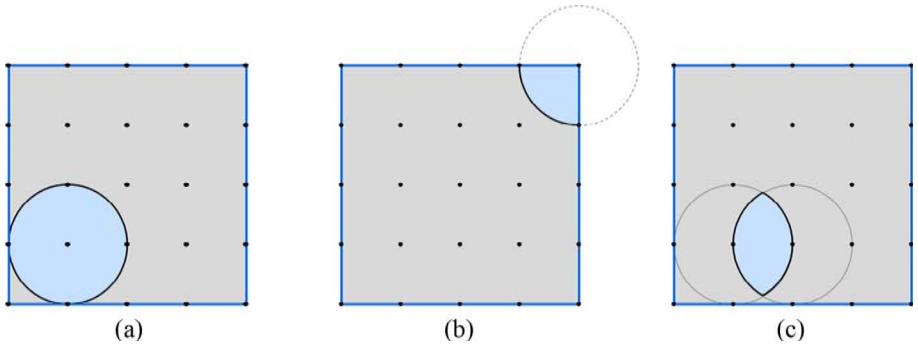

Fig. 2. Sphere integration domains for the method of finite spheres: (a) interior sphere, (b) boundary sphere, and (c) sphere overlap region.

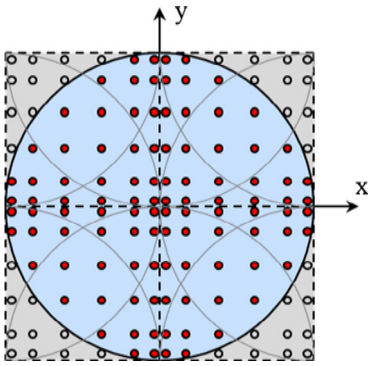

Fig. 3. Piecewise Gauss–Legendre quadrature rule for an interior sphere.

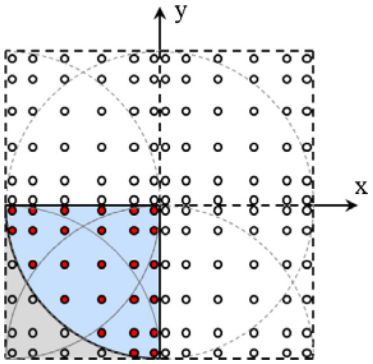

Fig. 4. Piecewise Gauss–Legendre quadrature rule for a boundary sphere.

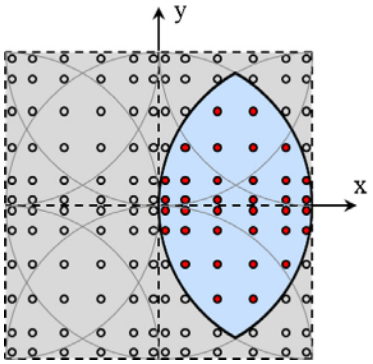

Fig. 5. Piecewise Gauss–Legendre quadrature rule for a sphere overlap region.

tion points, integration is performed using the subset of points in the sphere overlap region, indicated by red points.

Of course, there are multiple sphere overlaps for this interior sphere of interest, and each sphere overlap region considers a different subset of integration points and yields a unique nonzero sphere stiffness matrix. For a uniform arrangement of spheres in all directions, an interior sphere would have 26 overlap regions.

4. Implementation of the method of finite spheres

For the evaluation of the method of finite spheres, the procedure has been implemented in the user subroutine of ADINA. Therefore, the study is based on using the same sparse equation solver for the finite element method and the method of finite spheres and we can draw some valuable conclusions regarding the efficiency of the method.

4.1. Three-dimensional sphere element

For the displacement-based finite element method, we have three translational degrees of freedom per node, as shown in Fig. 6a. For the method of finite spheres, we have $3m$ degrees of freedom per node, as shown in Fig. 6b, where m is the number of terms in the local approximation space.

For three-dimensional linear static problems, a suitable local approximation space was given in Eq. (6). The local basis includes one constant term, three linear terms, and three quadratic terms, as shown in the Pascal pyramid in Fig. 7. Therefore, since $m = 7$, the sphere element has 21 nodal degrees of freedom.

We will compare solution times between the finite element method and the method of finite spheres for the three-dimensional linear elasticity numerical examples in Section 5. For the finite element solution, we use the 8-node linear brick element, and for the finite spheres solution, we use the linear sphere element, both of which are illustrated in Fig. 8. With three degrees of freedom per node in the finite element method, the linear brick element has a total of 24 degrees of freedom. In the method of finite spheres, the linear sphere element has a total of 21 degrees of freedom since the nodal degrees of freedom are the local element degrees of freedom.

For the method of finite spheres, the global structure stiffness matrix is a banded matrix with contributions from interior spheres, boundary spheres, and sphere overlap regions. A typical layout of the global structure stiffness matrix for the method of finite spheres is illustrated in Fig. 9, where the square matrices along the main diagonal correspond to the sphere element itself, either an interior sphere or a boundary sphere, e.g., $\underline{K}_{II}$, and the square matrices not along the main diagonal correspond to sphere overlap regions, e.g., $\underline{K}_{IJ}$, which are nonzero only when the spheres corresponding to nodes I and J overlap. The system of equations is

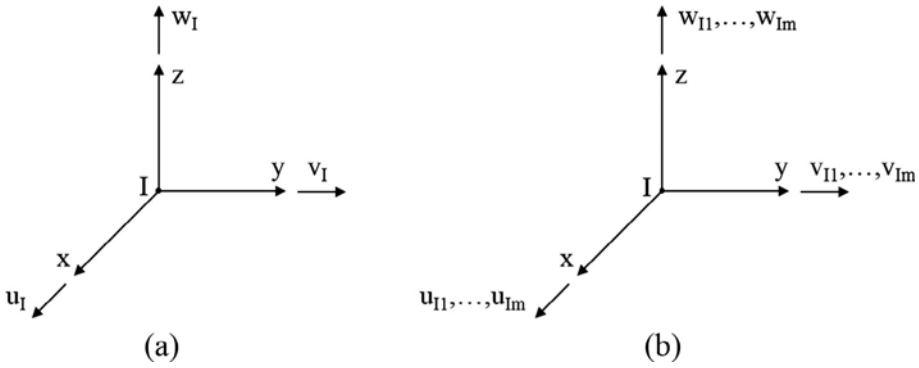

Fig. 6. (a) Finite element nodal degrees of freedom and (b) finite sphere nodal degrees of freedom.

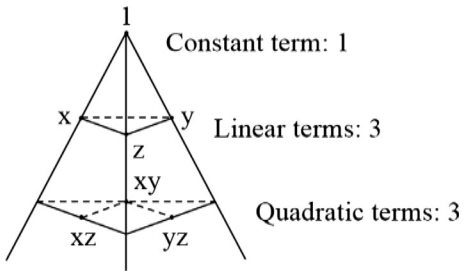

Fig. 7. Pascal pyramid representing the terms in the local approximation space for the sphere element.

solved in the same manner as in the standard finite element method.

4.2. Implementation in ADINA

A flowchart of the implementation of the method of finite spheres in ADINA is shown in Fig. 10. The first step is to read the nodal point data (number of nodal points, coordinates, radius, and essential boundary conditions) and element data (natural boundary conditions and material properties) from an ADINA data file. This data file is very similar to the one used for a finite element analysis, except that we no longer require a connectivity array relating the assemblage degrees of freedom to the element local

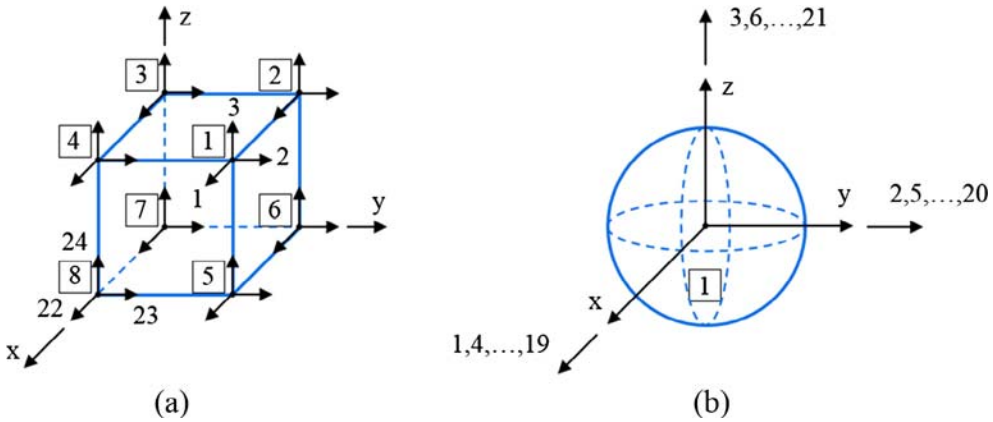

Fig. 8. (a) Linear brick element and (b) linear sphere element.

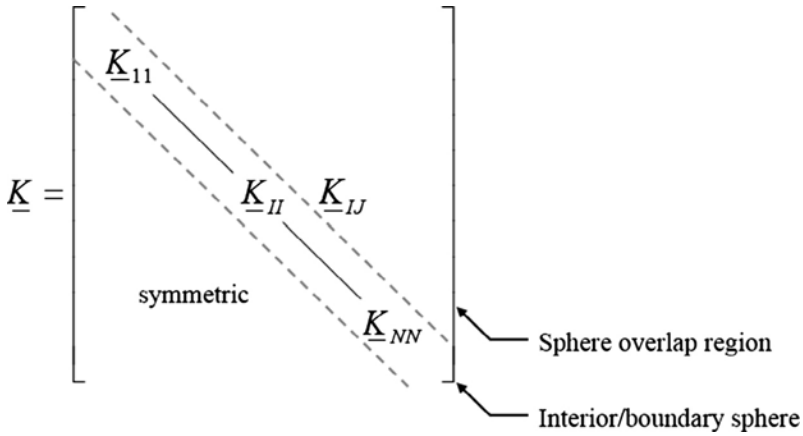

Fig. 9. Typical layout of structure stiffness matrix for the method of finite spheres.

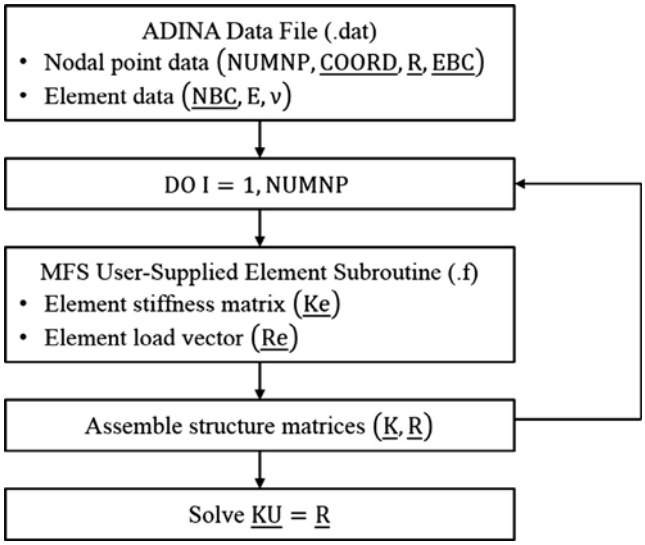

Fig. 10. Flowchart of method of finite spheres linear static analysis in ADINA.

degrees of freedom. The program then loops over every sphere for its element matrices to be assembled into the global structure matrices, where the element matrices already calculated are directly used or new element matrices are calculated. The nodal unknowns can then be determined by solving the system of equations using the ADINA equation solver. Post-processing of these results provides displacements, strains, and stresses throughout the problem domain. The complete process is like in a traditional finite element analysis.

5. Numerical results

In this section we consider the solutions of three increasingly more complex three-dimensional analysis problems and compare the solution times used in the standard finite element method and the method of finite spheres. In each case, we use the finest mesh finite element solution as the reference solution for comparison.

5.1. Problem 1: short cantilever beam with square solid section

We consider the short cantilever beam problem shown in Fig. 11.

The problem is solved using three discretizations for both the method of finite spheres and the finite element method, as shown in Fig. 12. For each sphere discretization, the sphere arrangement is uniform with equal radius size. For the finite element method, we use a sequence of uniform meshes consisting of 8-node linear brick elements. The mesh refinement involves subdividing each brick element into eight brick elements so that the coarser mesh will be embedded in the finer mesh, so we expect monotonic convergence [1].

The results for the MFS and FEM discretizations are given in Table 1. All three MFS discretizations provide results with strain energy errors within 9%. The time multiplier for MFS3 is 11.31, corresponding to a strain energy error of 0.48% which is close to negligible. We observe that a lower number of nodes can be used in the method of finite spheres to obtain comparable accuracy with the finite element method.

The convergence of strain energy for both methods is shown in Fig. 13. We observe that for a radius size in the method of finite spheres equal to element size in the finite element method, the method of finite spheres provides better accuracy based on the strain energy error norm with respect to the reference solution. Another important observation is that the method of finite spheres exhibits a similar rate of convergence (slope of convergence curve) as seen in the standard finite element method.

The transverse displacement contour plot calculated using the MFS3 discretization is shown in Fig. 14, with sphere centers denoted by the red nodes.

The z-displacement results and the predicted longitudinal normal stresses along Line 1, defined in Fig. 11, are shown in Figs. 15 and 16, respectively. Good solution accuracy is observed, except for (in this and the subsequent analyses) the nonphysical stresses in the mathematical model at the end regions.

5.2. Problem 2: short cantilever beam with square hollow section

The next structure considered is the short cantilever beam with a square hollow section, shown in Fig. 17.

The discretizations for the method of finite spheres and the finite element method are shown in Fig. 18. To arrive at the discretization from the square solid section, we simply remove the spheres that no longer are in the geometry domain of the hollow section. As before, the discretizations for the finite element method involve subdividing the 8-node brick elements into eight smaller brick elements, with the finest finite element discretization used as the reference solution.

The results for the MFS and FEM discretizations are summarized in Table 2. All three MFS discretizations provide results with strain energy errors within 7%. The time multiplier for MFS3 is 6.54, corresponding to a strain energy error of 1.04%. For this problem

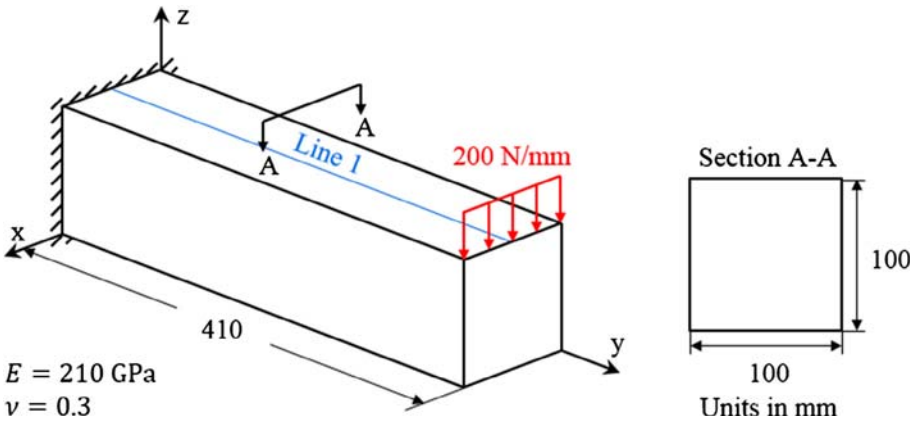

Fig. 11. Problem 1: short cantilever beam with square solid section.

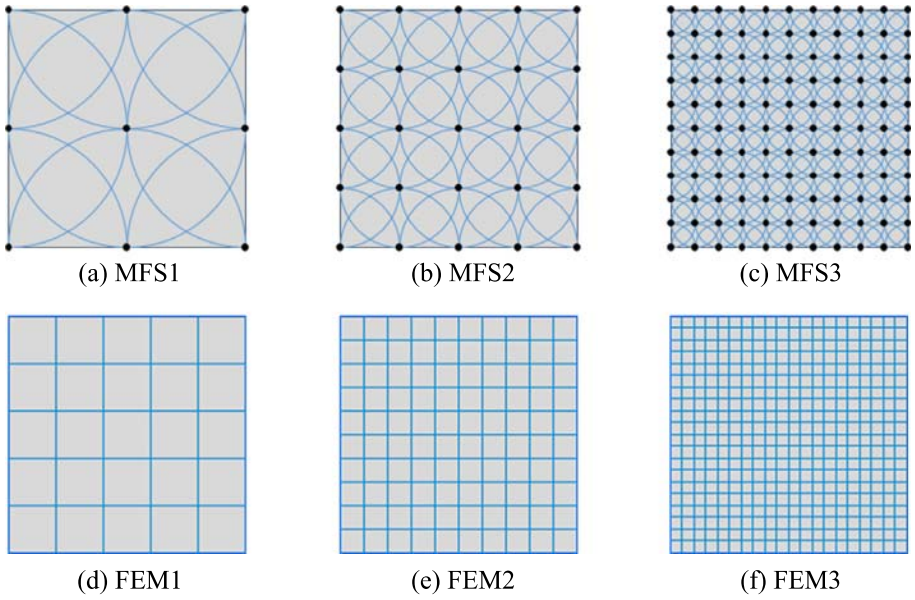

Fig. 12. MFS and FEM discretizations at Section A-A for Problem 1.

Table 1
Problem 1 strain energy errors and time multipliers for MFS and FEM discretizations (as compared to FEM3 reference solution).

	Number of nodes	Number of degrees of freedom	Strain energy error (%)	Time multiplier
MFS1	90	1890	8.19	0.08
MFS2	450	9450	2.83	0.37
MFS3	5082	106,722	0.48	11.31
FEM1	756	2160	3.55	0.01
FEM2	4961	14,520	1.06	0.04
FEM3	35,721	105,840	–[a]	–[a]

[a] FEM3: strain energy (N mm) = 2753.9; time (s) = 25.97.

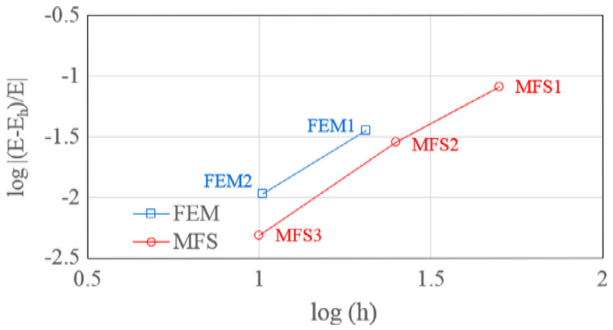

Fig. 13. Problem 1 convergence of strain energy.

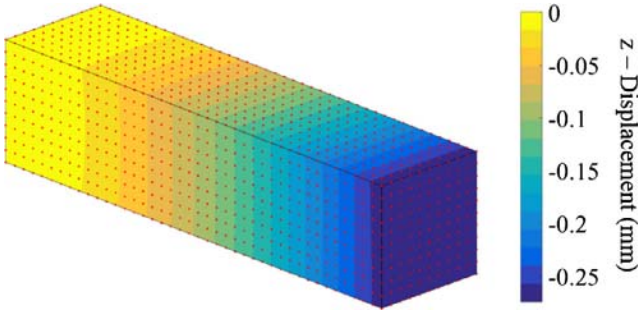

Fig. 14. Problem 1 transverse displacement contour plot for MFS3.

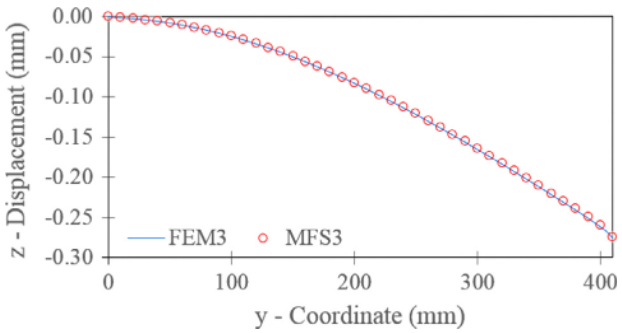

Fig. 15. Problem 1 transverse displacement along Line 1.

solution, the time multiplier indicates that the solution using the method of finite spheres is about one order of magnitude slower than the finite element method if a one percent strain energy error is accepted as small enough, but between one and two orders of magnitude slower if more accuracy is required using the method of finite spheres.

The convergence of strain energy for both methods is shown in Fig. 19. The method of finite spheres exhibits better accuracy compared to the finite element method when equal finite sphere and finite element sizes are considered. Furthermore, the method of finite spheres exhibits a similar rate of convergence as the finite element method, since the degree of polynomial completeness is the same for both the linear sphere element and linear brick element.

The calculated transverse displacement contour plot using the MFS3 discretization is shown in Fig. 20, with sphere centers denoted by the red nodes.

The transverse displacements along Line 1 (see Fig. 17) for the hollow structural section are larger than for the solid section, as expected, and the results using the two methods are in agreement, as shown in Fig. 21. The predicted longitudinal normal stresses along Line 1 are shown in Fig. 22, and again we see that the method of finite spheres provides good results.

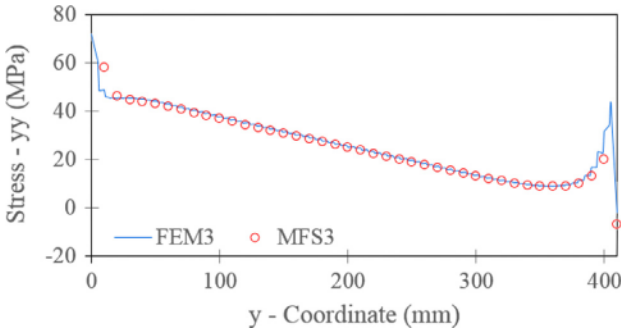

Fig. 16. Problem 1 longitudinal normal stress along Line 1.

5.3. Problem 3: machine tool jig

The final problem we solve is the cantilevered machine tool jig subjected to loading shown in Fig. 23. Due to the curved boundaries, discretization using finite elements is no longer as straightforward as for the previous two problems. This numerical example was obtained from an in-depth study of the solution of the problem using different hierarchical models from a beam model, to a shell model, to the three-dimensional elasticity model [35].

The discretizations for both methods are shown in Fig. 24. The method of finite spheres discretization for the problem solution is obtained from the discretization used in Section 5.2, by removing the spheres that have center coordinates in the volume of the

Table 2
Problem 2 strain energy errors and time multipliers for MFS and FEM discretizations (as compared to FEM3 reference solution).

	Number of nodes	Number of degrees of freedom	Strain energy error (%)	Time multiplier
MFS1	80	1680	6.87	0.68
MFS2	288	6048	4.04	2.38
MFS3	3024	63,504	1.04	6.54
FEM1	840	2400	4.81	0.01
FEM2	4920	14,400	1.52	0.05
FEM3	32,400	96,000	–[a]	–[a]

[a] FEM3: strain energy (N mm) = 4096.9; time (s) = 11.64.

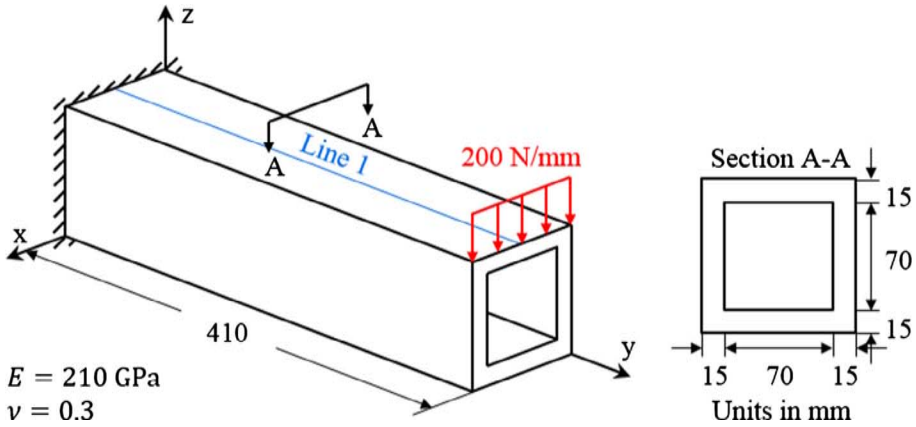

Fig. 17. Problem 2: short cantilever beam with square hollow section.

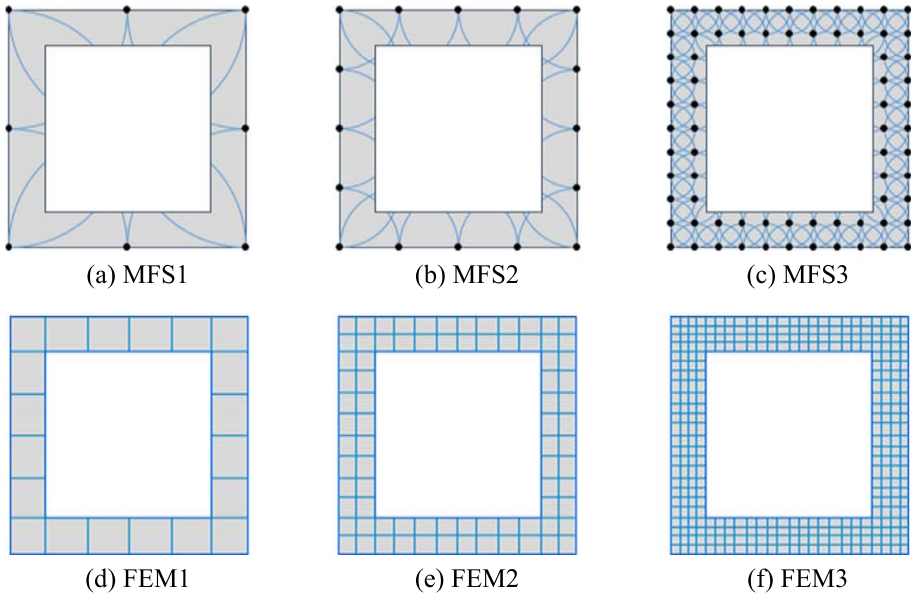

Fig. 18. MFS and FEM discretizations at Section A-A for Problem 2.

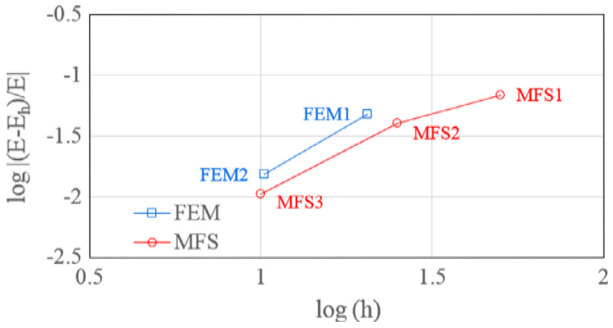

Fig. 19. Problem 2 convergence of strain energy.

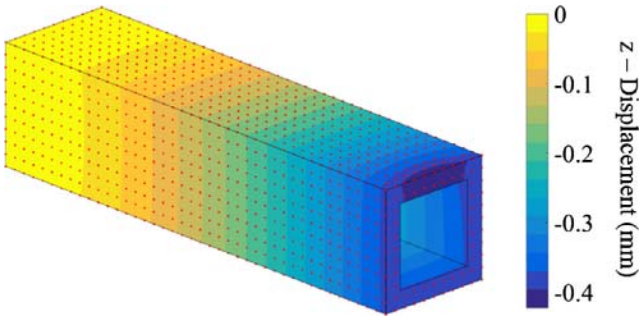

Fig. 20. Problem 2 transverse displacement contour plot for MFS3.

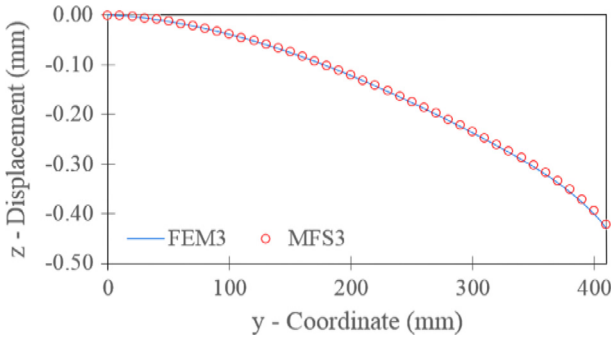

Fig. 21. Problem 2 transverse displacement along Line 1.

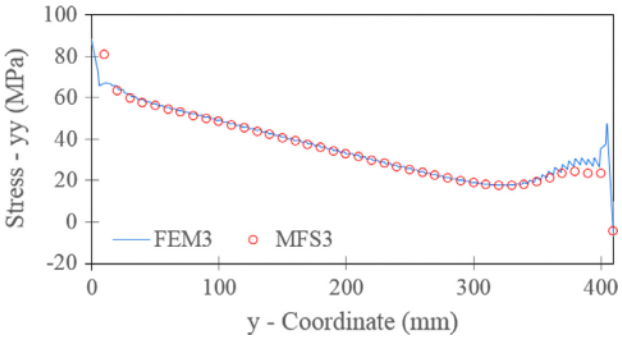

Fig. 22. Problem 2 longitudinal normal stress along Line 1.

machine tool jig cutout. As in the previous solutions, the finite element discretizations use the 8-node brick element, and each mesh refinement involves subdividing a brick element into eight smaller brick elements.

The results for the MFS and FEM discretizations are summarized in Table 3. For this problem solution, strain energy errors are within 30%, much larger than in the previous numerical examples. The coarse MFS discretizations do not accurately capture the stiffness of the structure leading to inaccurate displacements and large errors in the strain energy. The strain energy error for MFS3 is 4.27%, corresponding to a time multiplier of 7.59. Hence the solution time for the method of finite spheres is for this problem between one and two orders of magnitude larger than when using the finite element method for the same level of accuracy.

The convergence in strain energy for both methods is shown in Fig. 25.

The transverse displacement contour plot predicted using the MFS3 discretization is shown in Fig. 26.

Fig. 27 shows the z-displacement results for the method of finite spheres along Line 1, defined in Fig. 23. The predicted longitudinal normal stress results by both methods are also in agreement, as shown in Fig. 28.

For the machine tool jig problem, we next show a comparison between the method of finite spheres and the finite element method using the 27-node element. For the three FEM discretizations, the 8-node finite element is simply replaced by the 27-node finite element, with the finest discretization used as the reference solution. The results for the MFS and FEM discretizations are summarized in Table 4. Since the 27-node element reference solution is more accurate than the 8-node element reference solution, strain energy errors for the method of finite spheres are slightly larger. However, time multipliers are drastically reduced since the solution time for the 27-node element reference solution is roughly 150 times longer than for the 8-node element reference solution. MFS3 has a strain energy error of 5.82% corresponding to a time multiplier of 0.05. Computational efficiency comparisons

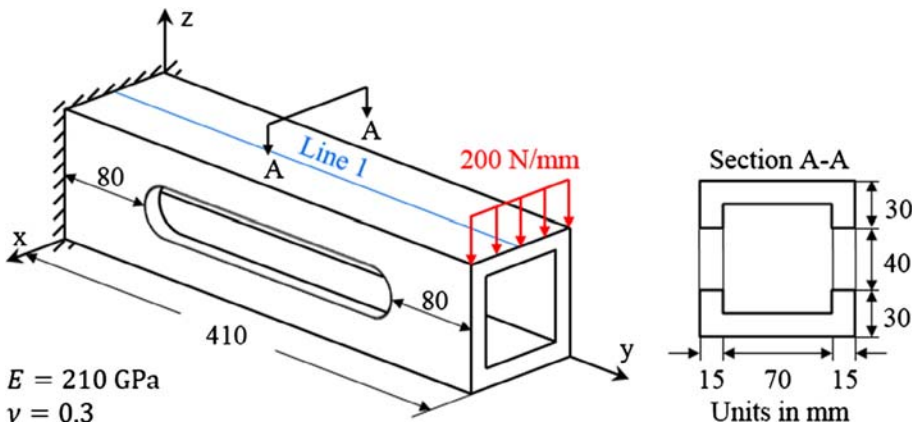

Fig. 23. Problem 3: machine tool jig.

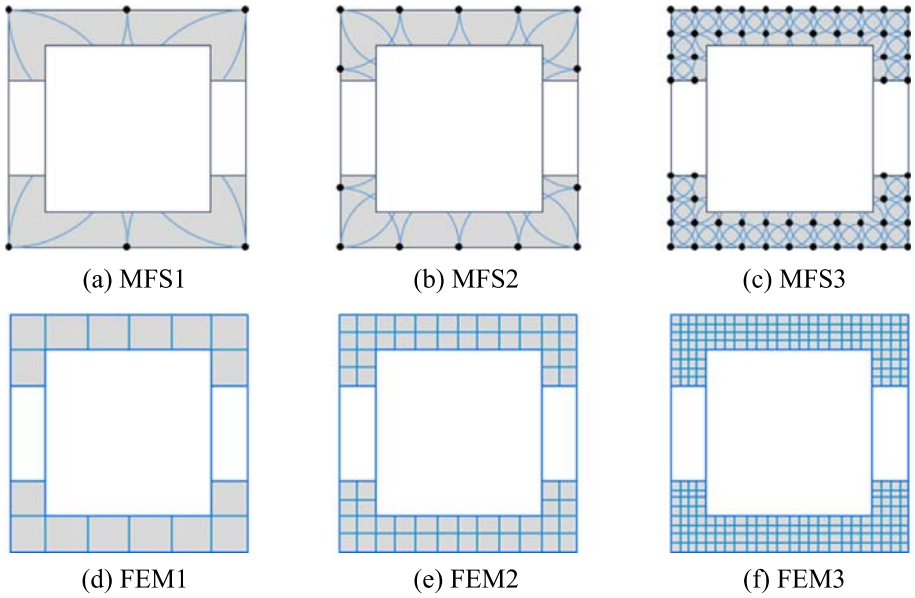

Fig. 24. MFS and FEM discretizations at Section A-A for Problem 3.

Table 3
Problem 3 strain energy errors and time multipliers for MFS and FEM discretizations (as compared to FEM3 reference solution).

	Number of nodes	Number of degrees of freedom	Strain energy error (%)	Time multiplier
MFS1	68	1428	29.92	1.22
MFS2	268	5628	17.24	4.53
MFS3	2736	57,456	4.27	7.59
FEM1	1060	3060	13.03	0.01
FEM2	6018	17,694	3.57	0.09
FEM3	38,950	115,650	–[a]	–[a]

[a] FEM3: strain energy (N mm) = 10185.1; time (s) = 8.99.

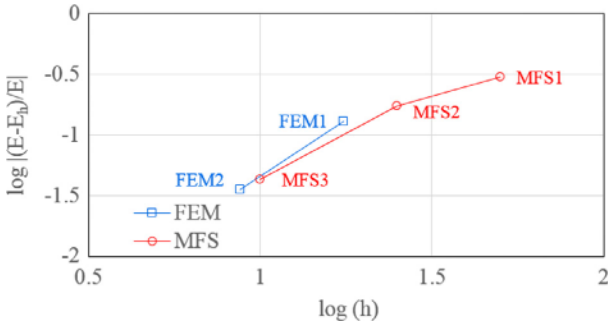

Fig. 25. Problem 3 convergence of strain energy.

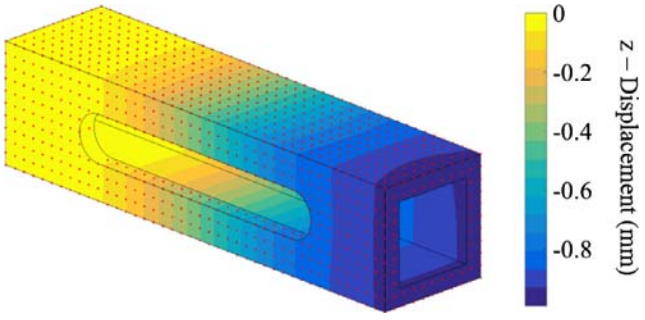

Fig. 26. Problem 3 transverse displacement contour plot for MFS3.

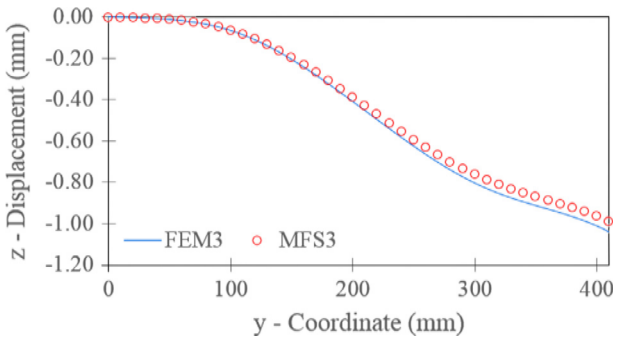

Fig. 27. Problem 3 transverse displacement along Line 1.

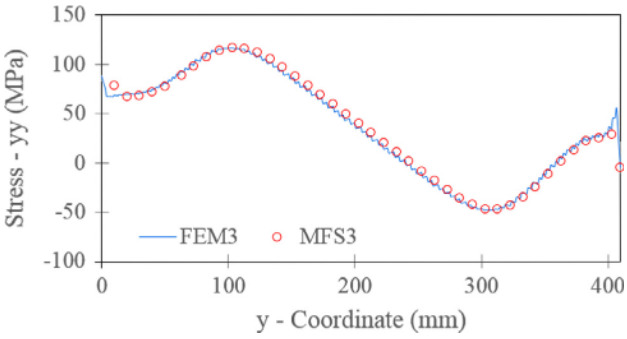

Fig. 28. Problem 3 longitudinal normal stress along Line 1.

Table 4
Problem 3 strain energy errors and time multipliers for MFS and FEM discretizations (as compared to FEM3 reference solution) with 27-node finite element.

	Number of nodes	Number of degrees of freedom	Strain energy error (%)	Time multiplier
MFS1	68	1428	31.05	0.01
MFS2	268	5628	18.58	0.03
MFS3	2736	57,456	5.82	0.05
FEM1	6018	17,694	1.13	<0.01
FEM2	38,950	115,650	0.27	0.02
FEM3	276,174	824,202	–[a]	–[a]

[a] FEM3: strain energy (N mm) = 10352.9; time (s) = 1371.97.

should be for the same level of accuracy, and by extrapolation we find that the method of finite spheres solution is around one order of magnitude slower than the finite element solution. However, here we used the linear sphere based on Eq. (6) and another comparison would involve the full quadratic terms in the local approximation space of the method of finite spheres.

The convergence in strain energy for the method of finite spheres and the finite element method using the 27-node element is shown in Fig. 29. In contrast to previous examples using the 8-node finite element, the finite element method is more accurate than the method of finite spheres for equal element size to radius size. This is expected since the 27-node element has polynomial completeness of degree two while the linear sphere element has polynomial completeness of degree one. Therefore, also a higher rate of convergence is observed for the 27-node finite element results.

The transverse displacement and longitudinal normal stress results are shown in Figs. 30 and 31, respectively. The transverse displacement results of the MFS3 solution differ slightly from the reference solution. The longitudinal normal stress results are in agreement, but unlike the results with the 8-node finite element, there are no stress discontinuities using the 27-node element.

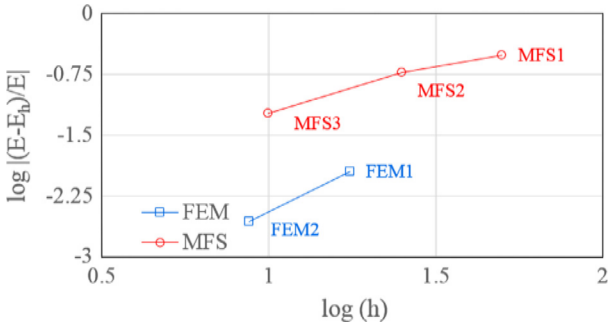

Fig. 29. Problem 3 convergence of strain energy with 27-node finite element.

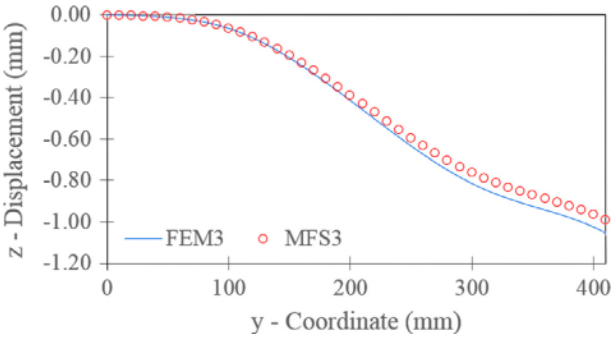

Fig. 30. Problem 3 transverse displacement along Line 1 with 27-node finite element.

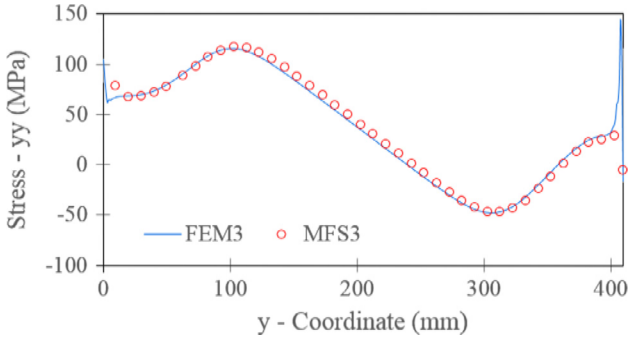

Fig. 31. Problem 3 longitudinal normal stress along Line 1 with 27-node finite element.

Based on the analysis of the machine tool jig problem, the method of finite spheres is capable of obtaining an accurate solution, with computational times between one and two orders of magnitude slower than the finite element method based on the 8-node finite element, and computational times around one order of magnitude slower based on the 27-node finite element.

6. Concluding remarks

The objective of this paper was to assess the reliability and efficiency of the method of finite spheres for the solution of three-dimensional linear elasticity problems. We presented the basic theory and formulation used and then obtained solutions using the method of finite spheres for comparison with the traditional finite element method. For these comparisons, the method of finite spheres was implemented in the user subroutine of the program ADINA.

The solution time comparisons showed that the method of finite spheres is about one to two orders of magnitude slower than the finite element method. However, for the numerical examples studied, the discretizations of the domains were based on a regular arrangement of spheres with identical element stiffness matrices for certain spheres. We used this attribute to calculate the element stiffness matrices for unique spheres only once for the assembly of all such sphere contributions in the structure stiffness matrix. Of course, this is only possible in linear analysis, and when many identical spheres are used.

Based on our research, the method of finite spheres is a promising method for the solution of three-dimensional linear elasticity problems. Advantages of this formulation include avoiding mesh generation and element distortion. However, additional research is needed to enable greater computational efficiency. One area that is particularly suitable for improving the efficiency of the method is distributed memory parallel processing. Sphere element stiffness calculations are the primary computational cost for the method of finite spheres, but these calculations can be performed independently. By allocating spheres to multiple cores, more computations can be performed in parallel leading to faster solution times as well as more efficient memory usage. Furthermore, having emphasized that the method of finite spheres is essentially an overlapping finite element method, it is important to note that the method is a particularly attractive meshless method for coupling with the finite element method, as has been shown for two-dimensional problems [20,23]. The basic idea is that the finite spheres can be used within a standard finite element analysis as another element type, employed in regions that are difficult to mesh or in the new meshing scheme detailed in Ref. [36].

References

[1] Bathe KJ. Finite element procedures. Prentice Hall; 1996.
[2] Lee NS, Bathe KJ. Effects of element distortions on the performance of isoparametric elements. Int J Numer Meth Eng 1993;36:3553–76.
[3] Belytschko T, Krongauz Y, Organ D, Fleming M, Krysl P. Meshless methods: an overview and recent developments. Comput Methods Appl Mech Eng 1996;139:3–47.
[4] Liu GR. Meshfree methods: moving beyond the finite element method. CRC Press; 2002.
[5] Chen Y, Lee JD, Eskandarian A. Meshless methods in solid mechanics. Springer; 2006.
[6] Monaghan JJ. An introduction to SPH. Comput Phys Commun 1988;48:89–96.
[7] Liu MB, Liu GR. Smoothed particle hydrodynamics (SPH): an overview and recent developments. Arch Comput Methods Eng 2010;17:25–76.
[8] Nayroles B, Touzot G, Villon P. Generalizing the finite element method: diffuse approximation and diffuse elements. Comput Mech 1992;10:307–18.
[9] Belytschko T, Lu YY, Gu L. Element-free Galerkin methods. Int J Numer Meth Eng 1994;37:229–56.

[10] Lu YY, Belytschko T, Gu L. A new implementation of the element free Galerkin method. Comput Methods Appl Mech Eng 1994;113:397–414.
[11] Belytschko T, Krysl P, Krongauz Y. A three-dimensional explicit element-free Galerkin method. Int J Numer Methods Fluids 1997;24:1253–70.
[12] Barry W, Saigal S. A three-dimensional element-free Galerkin elastic and elastoplastic formulation. Int J Numer Meth Eng 1999;46:671–93.
[13] Atluri SN, Zhu T. A new meshless local Petrov–Galerkin approach in computational mechanics. Comput Mech 1998;22:117–27.
[14] Atluri SN, Kim HG, Cho JY. A critical assessment of the truly meshless local Petrov–Galerkin (MLPG), and local boundary integral equation (LBIE) methods. Comput Mech 1999;24:348–72.
[15] Han ZD, Atluri SN. Meshless local Petrov–Galerkin (MLPG) approaches for solving 3D problems in elasto-statics. CMES-Comput Model Eng Sci 2004;6:169–88.
[16] De S, Bathe KJ. The method of finite spheres. Comput Mech 2000;25:329–45.
[17] De S, Bathe KJ. Towards an efficient meshless computational technique: the method of finite spheres. Eng Comput 2001;18:170–92.
[18] De S, Bathe KJ. Displacement/pressure mixed interpolation in the method of finite spheres. Int J Numer Meth Eng 2001;51:275–92.
[19] De S, Bathe KJ. The method of finite spheres with improved numerical integration. Comput Struct 2001;79:2183–96.
[20] Hong JW, Bathe KJ. Coupling and enrichment schemes for finite element and finite sphere discretizations. Comput Struct 2005;83:1386–95.
[21] Macri M, De S. Enrichment of the method of finite spheres using geometry-independent localized scalable bubbles. Int J Numer Meth Eng 2007;69:1–32.
[22] Macri M, De S, Shephard MS. Hierarchical tree-based discretization for the method of finite spheres. Comput Struct 2003;81:789–803.
[23] Macri M, De S. Towards an automatic discretization scheme for the method of finite spheres and its coupling with the finite element method. Comput Struct 2005;83:1429–47.
[24] Banihani S, De S. Development of a genetic algorithm-based lookup table approach for efficient numerical integration in the method of finite spheres with application to the solution of thin beam and plate problems. Int J Numer Meth Eng 2006;67:1700–29.
[25] Ham S, Lai B, Bathe KJ. The method of finite spheres for wave propagation problems. Comput Struct 2014;142:1–14.
[26] Melenk JM, Babuška I. The partition of unity finite element method: basic theory and applications. Comput Methods Appl Mech Eng 1996;139:289–314.
[27] Babuška I, Melenk JM. The partition of unity method. Int J Numer Meth Eng 1997;40:727–58.
[28] Duarte CA, Oden JT. H-p clouds – an h-p meshless method. Numer Methods Partial Diff Equat 1996;12:673–705.
[29] Dolbow J, Belytschko T. Numerical integration of the Galerkin weak form in meshfree methods. Comput Mech 1999;23:219–30.
[30] Carpinteri A, Ferro G, Ventura G. The partition of unity quadrature in meshless methods. Int J Numer Meth Eng 2002;54:987–1006.
[31] Mazzia A, Ferronato M, Pini G. A comparison of numerical integration rules for the meshless local Petrov–Galerkin method. Numer Algorithms 2007;45:61–74.
[32] Babuška I, Banerjee U, Osborn JE, Li Q. Quadrature for meshless methods. Int J Numer Meth Eng 2008;76:1434–70.
[33] Babuška I, Banerjee U, Osborn JE, Zhang Q. Effect of numerical integration on meshless methods. Comput Methods Appl Mech Eng 2009;198:2886–97.
[34] Beissel S, Belytschko T. Nodal integration of the element-free Galerkin method. Comput Methods Appl Mech Eng 1996;139:49–74.
[35] Bucalem ML, Bathe KJ. The mechanics of solids and structures – hierarchical modeling and the finite element solution. Springer; 2011.
[36] Bathe KJ, Zhang L. The finite element method with overlapping elements – a new paradigm for CAD driven simulations [in preparation].